

In-situ Electrical Resistance and X-ray Tomography Study of Copper-Tin Polymer Composites during Thermal Annealing

Qing Yang, Megan Hoarfrost Beers, Min Zheng, Richard Lloyd, Ting Gao, Dilworth Parkinson

Dr. Qing Yang, Dr. Dilworth Parkinson

Advanced Light Source, Lawrence Berkeley National Laboratory

Berkeley, CA 94720, USA

Dr. Megan Hoarfrost Beers, Dr. Min Zheng, Richard Lloyd, Dr. Ting Gao

Tyco Electronics Corporation, a TE Connectivity Ltd. company

Menlo Park, CA, USA

Correspondence to:

Dr. Dilworth Parkinson (Email: dyparkinson@lbl.gov)

Dr. Megan Hoarfrost Beers (Email: megan.beers@te.com)

Abstract

In-situ electrical conductivity and X-ray tomography experiments are conducted on a conductive polymer composite containing polyvinylidene fluoride (PVDF) copolymer, copper (Cu) and tin (Sn) during thermal annealing. During annealing, the electrical resistivity drops by an order of magnitude, while X-ray tomography, electron microscopy and spectroscopy results show increasingly homogeneous dispersion of Sn in the conductive filler network, accompanied by the formation of Cu-Sn intermetallic around Cu and Sn particles. This study provides detailed insight into the morphological origins of the beneficial effect of thermal annealing on the electrical properties of conductive composites containing low melting metal fillers.

This is the author manuscript accepted for publication and has undergone full peer review but has not been through the copyediting, typesetting, pagination and proofreading process, which may lead to differences between this version and the [Version record](#). Please cite this article as [doi:10.1002/app.45399](https://doi.org/10.1002/app.45399).

Introduction

Composites with conductive fillers dispersed in a polymer matrix have found a wide range of applications, including electrical connections, electrodes, sensors, antistatic devices and electromagnetic interference (EMI) shielding. Benefiting from the properties of both polymers and conductive fillers, they have desirable mechanical flexibility, processability and chemical stability, while having adequate electrical conductivity.

In efforts to improve electrical conductivity without increasing volume fraction of the filler, many studies have shown that thermal annealing at temperatures higher than the glass transition temperature of the polymers, such as polypropylene, Nylon, PMMA and polystyrene, can affect the distribution, morphology and therefore percolation of the fillers.^{1–7} The primary mechanism behind the annealing effect is the viscoelastic relaxation of the polymer that leads to rearrangement of filler particles and better interconnected conductive network. Furthermore, adding low-melting metal fillers into the conductive filler network can also help improve conductivity by introducing improved inter-particle contact.^{7–14} However, the effect of thermal annealing on composites containing low-melting fillers has only been considered in one previous studies performed by the authors.⁷ This study provides an in-depth look at how particle composition, morphology, and distribution change during thermal annealing in a polymeric composite containing solid as well as low-melting conductive metal fillers, and explores how these changes affect the electrical properties of the composite.

In addition to providing 3D compositional and morphological information, synchrotron-based X-ray tomography allows for fast scanning speed comparable to the time scale of the annealing process thanks to its extremely high flux. In-situ experiments are thus possible, and utilized in

this study to visualize and quantify the dynamic changes in morphology and composition of composite fillers during thermal treatment.

A separate in-situ experiment is also utilized to track resistivity changes of the conductive composites under similar annealing conditions. Scanning electron microscopy (SEM) and energy dispersive spectroscopy (EDS) are also used to verify changes before and after annealing.

Experimental

The materials used in this work are the same as those used in Reference 7, where they are described in detail. Polyvinylidene fluoride (PVDF) copolymer composite samples filled with 24 vol% Cu and 16 vol% Sn were prepared. The dendritic Cu and the spherical Sn powders are approximately 26 μm and 10 μm in diameter, respectively. Their apparent bulk powder densities are 1.0 and 3.7 g/cm^3 , respectively. The total metal filler loading of 40 vol % was selected because it is much higher than the literature reported percolation threshold of 5–15 vol % for polymer composites filled with dendritic Cu.^{15,16} For commercial use, it is desirable for the conductivity to be homogeneous and stable, which is best accomplished by using a metal content well above the percolation threshold, hence the selection of 40 vol % filler loading. The powders were first compounded with PVDF copolymer resin (Kynar Flex®) for 10 min at 200 °C using a Brabender batch mixer with Sigma blades rotating at 40 rpm. The composite was then molded into stair-step shaped bar samples using a Haake MiniJet table-top injection molding system. The stair-step shaped bar samples are 100 mm long, 10 mm wide, and have three equally sized “stair-step” sections with thicknesses 0.5, 1, and 1.5 mm. The barrel temperature, at which the compounds were thermally equilibrated, was set to 225 °C, and the temperature of the mold

where the melt compound was injected, was set to 200 °C. Raw powders, compounding and molding conditions used in this study are detailed in a previous publication.⁷

Prior to in-situ conductivity measurements and tomographic imaging, as-molded samples were crosslinked via electron-beam crosslinking, using a beam energy of 1 MeV, a beam current between 1.2–4 mA, and a radiation dose of 29.5 Mrad. As a result of crosslinking, the samples do not flow during subsequent annealing experiments.

For in-situ electrical conductivity measurements, the center portion of a stair-step shaped bar sample was used (33 mm long, 10 mm wide, and 1 mm thick). Four-point resistivity measurements of the sample were made while the sample was inside a temperature-controlled oven (atmospheric environment) using Agilent Technologies digital multimeters and home-made test fixtures. Measurements were made along the length of the sample using clip probes spaced 11 mm apart on the sample, with a voltage of 10 V. Contact resistance between the probes and the sample was therefore eliminated by the separation of current and voltage electrodes.

In-situ tomographic imaging was performed at Beamline 8.3.2 of the Advanced Light Source at Lawrence Berkeley National Laboratory. A cuboid-shaped sample with dimensions of approximately 0.5 mm×0.5 mm×10 mm was cut from a molded stair-step shaped bar sample, and vertically mounted in a sample clip inside a heating assembly designed and made in-house, as shown in **Figure 1**. Heat was generated from two DC-powered heat cartridges inside a copper block at the bottom of the assembly. A 0.125-inch thick aluminum tubing was used as a secondary heat source fitted outside and above the heat source due to its good thermal conductivity and low absorption of hard X-rays. As a thermal insulation, glass fiber cloth (not shown) was taped around the aluminum tube (but leaving a window where the X-ray passes through). A PEEK cap was fitted on top of the aluminum tube to further reduce heat dissipation.

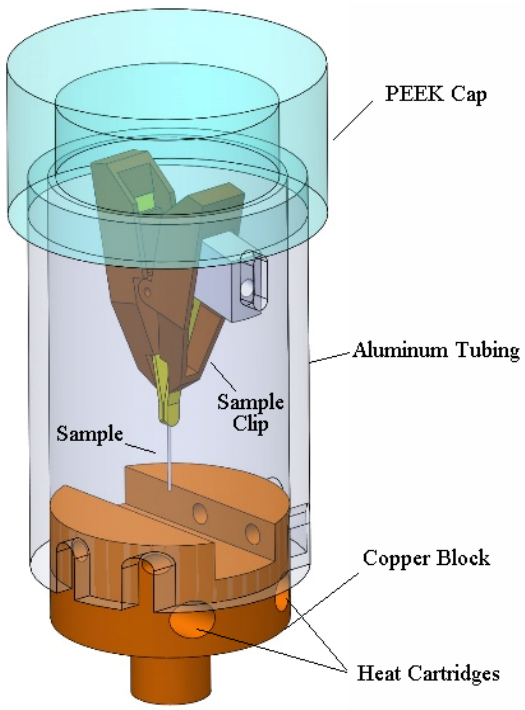


Figure 1. Schematic 3D drawing of the in-situ tomography test cell.

White light X-rays were used to provide higher flux (compared to monochromatic X-rays), allowing for faster imaging. A LuAG:Ce scintillator was used to convert X-rays to visible light, which was imaged with a 10x lens and a PCO.Edge sCMOS camera. Scans were acquired roughly every 12 minute as the sample was continuously rotated 180°. The image resolution is 2560×2160 pixels and the pixel size is 0.61 μm. A Model Based Iteration Reconstruction (MBIR) algorithm^{17,18} was used to perform tomographic reconstructions at the National Energy Research Scientific Computing Center (NERSC).

SEM with EDS analysis was performed on Cu-Sn composite samples using a JEOL 7000 with Oxford EDS detector, using 15kV conditions; AZtecEnergy software was utilized to analyze the material phases on the EDS mapping. XRD analysis was carried out using a Rigaku TTRAXIII instrument with a Cu X-ray resource. The Bragg-Brentano focusing method was chosen for the

sample scan; results were further analyzed using PDXL2 software from Rigaku for phase identification and whole pattern powder fitting.

Results and Discussion

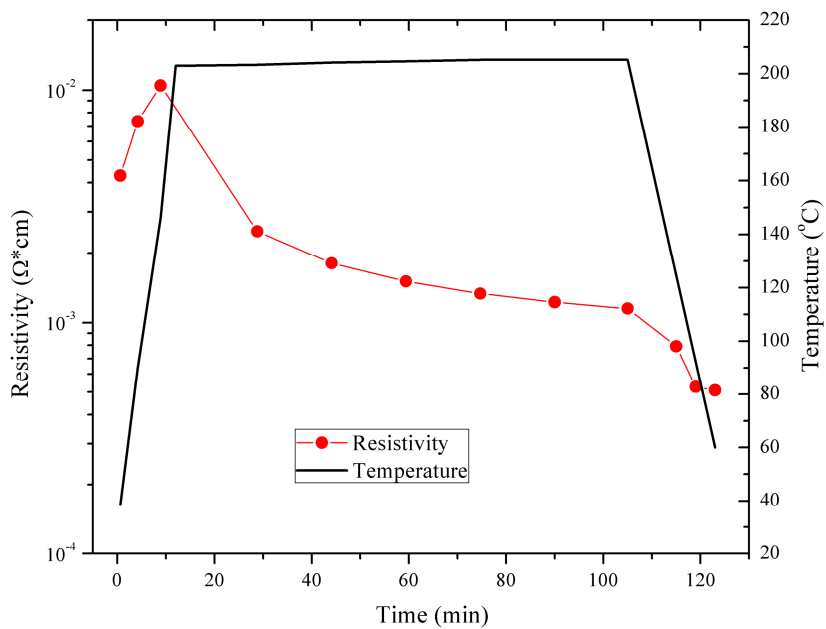


Figure 2. Resistivity evolution of an e-beamed, composite sample during thermal annealing in air. Error bars are estimated to be 5% based on knowledge of the equipment used.

Figure 2 shows the resistivity measurements of the composite during thermal annealing. An initial increase in resistivity is observed as the temperature ramps up to 205 $^{\circ}C$. This is likely caused by the reduction of inter-particle contact between fillers as a result of thermal expansion of the polymer, as well as volumetric expansion during melting of the crystalline regions of the polymer near 177 $^{\circ}C$. This crystalline-amorphous transition behavior has been utilized in devices such as positive temperature coefficient resettable devices for current surge and over-temperature protection.^{19,20}

Upon thermal equilibrium at 205 °C, the resistivity of the sample decreases with time. It is hypothesized that exposure to elevated temperatures near the melting temperature of Sn (232 °C) for extended periods of time facilitates better dispersion of Sn in the conductive filler network, leading to better coating of Cu particles and thus improved contact between particles. Note that the annealing temperature was selected to be below the melting temperature of Sn to prevent Sn from fully melting and separating out of the composite material during annealing. The annealing time was based on “ex-situ” experiments, wherein individual samples were annealed for different times, and their resistivities measured before and after. After about two hours, the observed decrease in resistivity leveled off. Upon cooling to room temperature, the sample exhibits a further decrease in resistivity, likely due to the compression and recrystallization of the polymer matrix. The temperature dependence of the resistivity of Cu and Sn is also a factor, but only contributes about 1% to the overall decrease in resistivity, according to their temperature coefficients. Overall, the resistivity of the composite drops by about an order of magnitude after annealing—consistent with ex-situ annealing experiments reported previously.⁷

Accepted Article

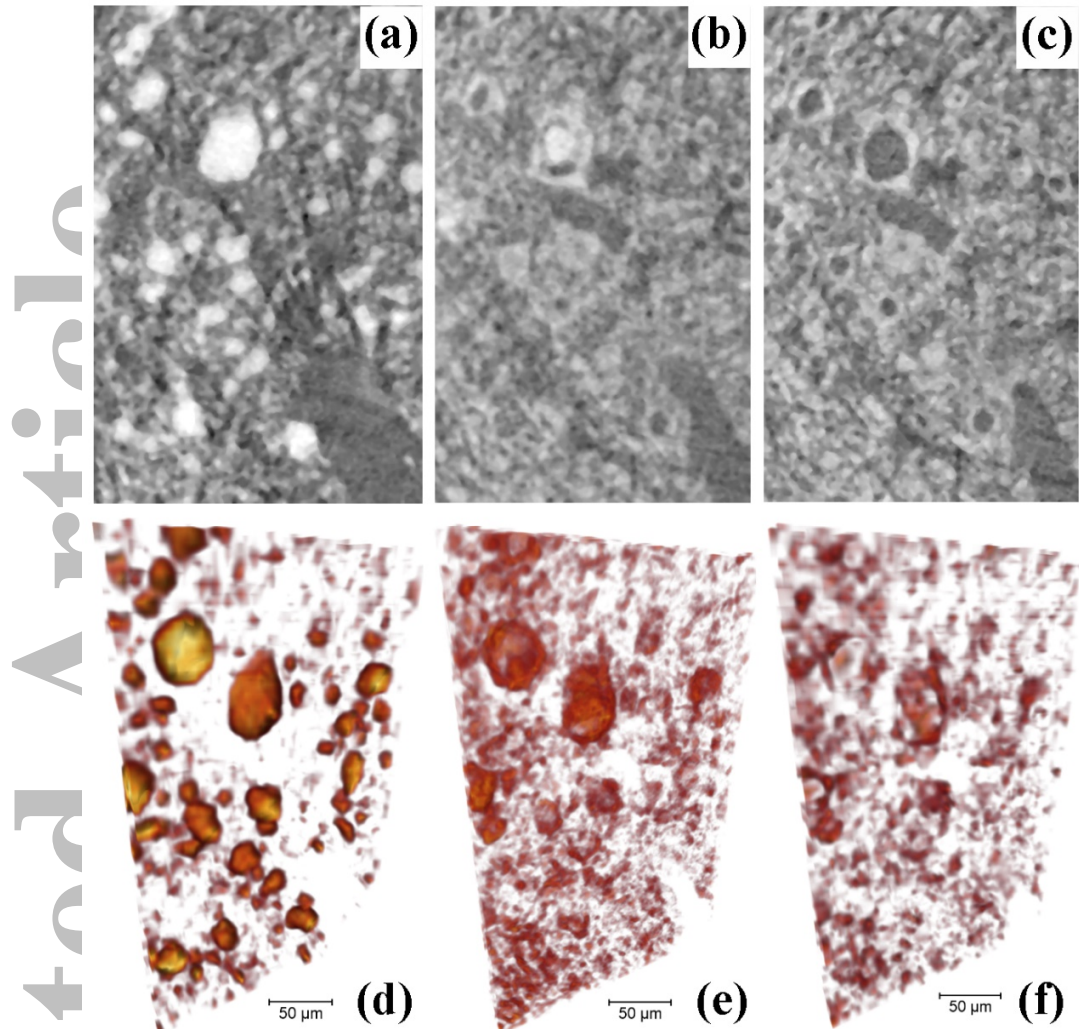


Figure 3. Tomographically reconstructed cross-sections and volume renderings of the composite (a)(d) before annealing, (b)(e) annealed at 210 °C for 60 min, and (c)(f) after 130 minutes of annealing. All image data sets were aligned, cropped and filtered in a same workflow using the Avizo 3D software (FEI Visualization Sciences Group), and the color map is based on X-ray absorption data of the sample.

In order to understand if and how microstructural changes are related to the resistivity improvement during annealing, in-situ tomographic experiments were conducted to provide dynamic, three-dimensional information about the composite microstructure. The resistivity of the sample prepared for the in-situ tomographic experiments before and after annealing was

measured to be $23 \Omega \cdot \text{cm}$ and $2.1 \times 10^{-3} \Omega \cdot \text{cm}$, respectively. These values are much higher than those shown in Figure 2, especially before annealing, because the sample is much smaller than the sample measured in the in-situ resistivity experiment ($0.5 \text{ mm} \times 0.5 \text{ mm} \times 10 \text{ mm}$ compared to $1 \text{ mm} \times 10 \text{ mm} \times 33 \text{ mm}$). Resistivity is generally an intrinsic property for homogeneous materials. However, the resistivity of the conductive composite depends on conductive pathways formed by distributed conductive particles. For small samples, the number and degree of connectedness of the conductive pathways are affected by the geometric limitations. But like the larger sample, a significant decrease in resistivity is observed before and after annealing.

With the help of a fiducial crack (visible in the bottom right portion of the region of interest), all data sets before, during and after annealing were aligned with one another. Sn has greater absorption than Cu, so Sn is seen as the brightest regions in the reconstructed images, where pixel values represent X-ray linear absorption coefficients. As shown in **Figure 3(a) and 3(d)**, large, presumably Sn, particles are present before annealing. After annealing for about one hour, many of these particles shrink in size, as seen in both the cross sectional view and the 3D visualization (Figure 3(b) and 3(e)), and Sn seems to be distributed more homogeneously throughout the sample, including in areas where there was no Sn before annealing. In addition, hollow structures form where the largest Sn particles were originally located. After 130 minutes of annealing (Figure 3(c) and 3(f)), most Sn particles are hardly distinguishable, and only “shell” structures are visible at locations where the largest Sn particles originally were observed.

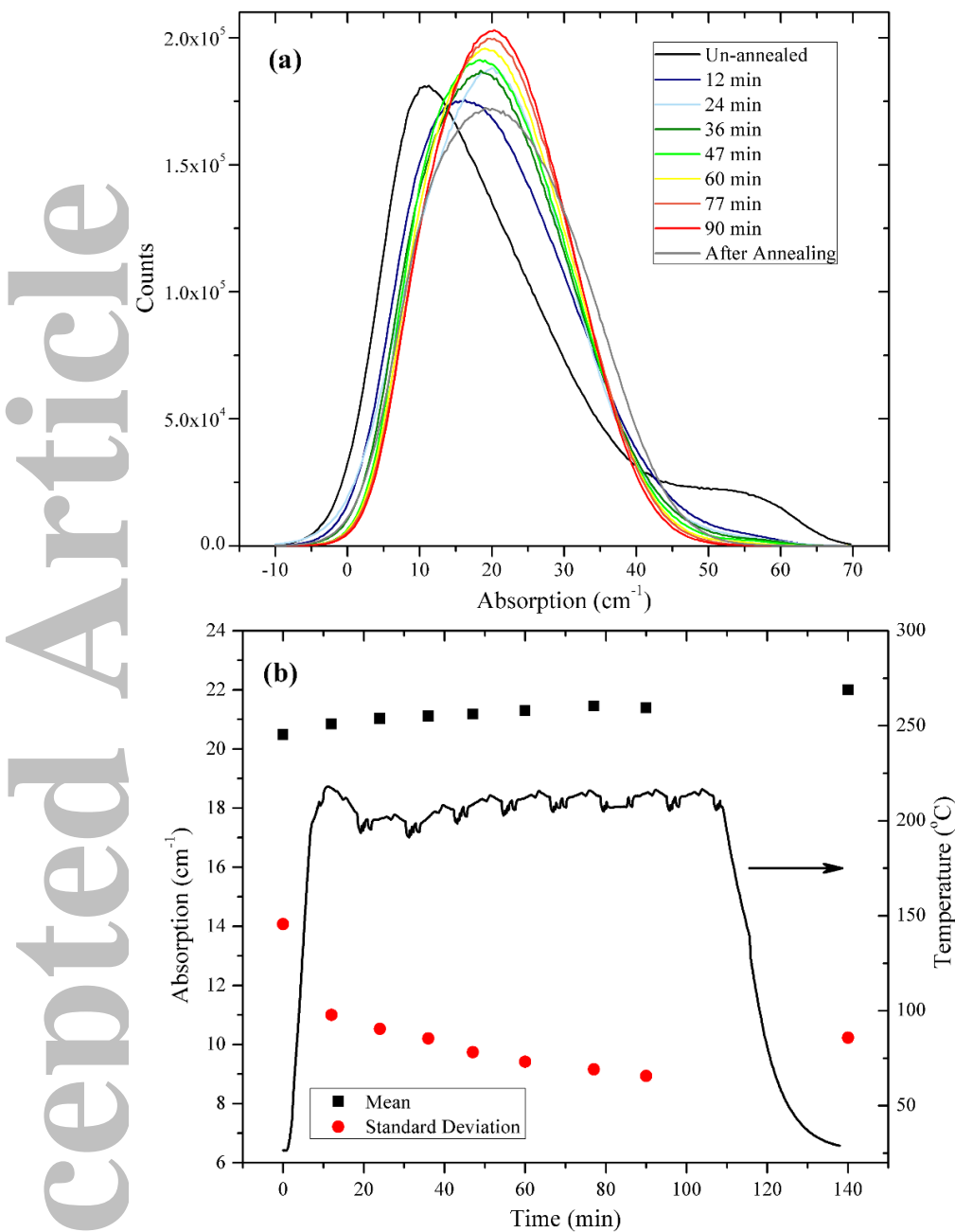


Figure 4. (a) Histograms of 3D images based on a representative volume of $336 \times 214 \times 49 \mu\text{m}^3$ of the composite sample successively annealed at 210°C . (b) Temperature profile of the in-situ annealing experiment and statistical analysis of all the corresponding image data sets.

In order to further understand the morphological changes observed, quantitative histogram analysis of the tomography absorption data was conducted on the same region of interest as shown in Figure 3 for nine successive annealing time points. As expected, the un-annealed sample has a noticeable high-intensity peak on its histogram around 55 cm^{-1} , as shown in **Figure 4(a)**, indicating large isolated Sn particles and poor dispersion. (The peak is close to the expected Sn absorption of ~ 58 , whereas Cu absorption is much lower.) The “rainbow” color-coded histograms show that the intensity of the peak near 55 cm^{-1} decreases and the distribution of X-ray absorption becomes narrower as the annealing time increases, indicating better dispersion of Sn and overall more homogeneous dispersion of metallic fillers in the composites annealed for longer times. The location of the main peak also shifts to higher absorption (from $\sim 10\text{ cm}^{-1}$ to $\sim 20\text{ cm}^{-1}$); that the main peak shifts to a more “central” value between the absorption values of pure Cu and Sn is further indication that Cu and Sn distribution become more homogeneous at the length scale of individual pixels ($0.61\text{ }\mu\text{m}$). These results are all consistent with ex-situ annealing experiments reported previously.⁷ Note that although the in-situ tomography data in this experiment cannot quantitatively differentiate Cu and Sn, it is a good assumption that the Cu filler network is relatively immobile due to its melting temperature being much higher than the annealing temperature. Therefore, Sn is considered to be the primary component undergoing movement and redistribution.

Statistical analysis shown in Figure 4(b) reveals that the standard deviation of the histogram drops from 14 to 9 upon annealing, a further indication that there is more homogeneous dispersion of the filler network within the region of interest as the annealing time increases. The small but steady increase in the mean absorption of the entire region of interest throughout the experiment is possibly due to mass transfer across the boundary of the region of interest,

especially around the fiducial crack. This may also contribute to the gradual shift of the histograms to higher X-ray absorption in Figure 4(a).

Interestingly, the histogram of the post-annealed sample exhibits a rather wide distribution compared to the distributions during annealing. The large increase in standard deviation observed for the post-annealed sample may be caused by thermal contraction and polymer crystallization upon cooling that make the metal filler distribution less homogenous. This is also consistent with the large decrease in standard deviation observed between 0 and 10 minutes during the initial stage of annealing.

Overall, the standard deviation of the absorption distribution decreases from 14 to 10 from pre-annealing to post-annealing. The more homogeneous distribution of Sn after annealing is thought to contribute strongly to the improvement in resistivity observed after annealing, by facilitating the formation of a better connected conductive network within the composite.

It is important to note that the % crystallinity of PVDF does not change significantly before and after annealing,⁷ which reinforces the argument that changes in Cu/Sn morphology and distribution are the main driving force behind the changes in electrical conductivity.

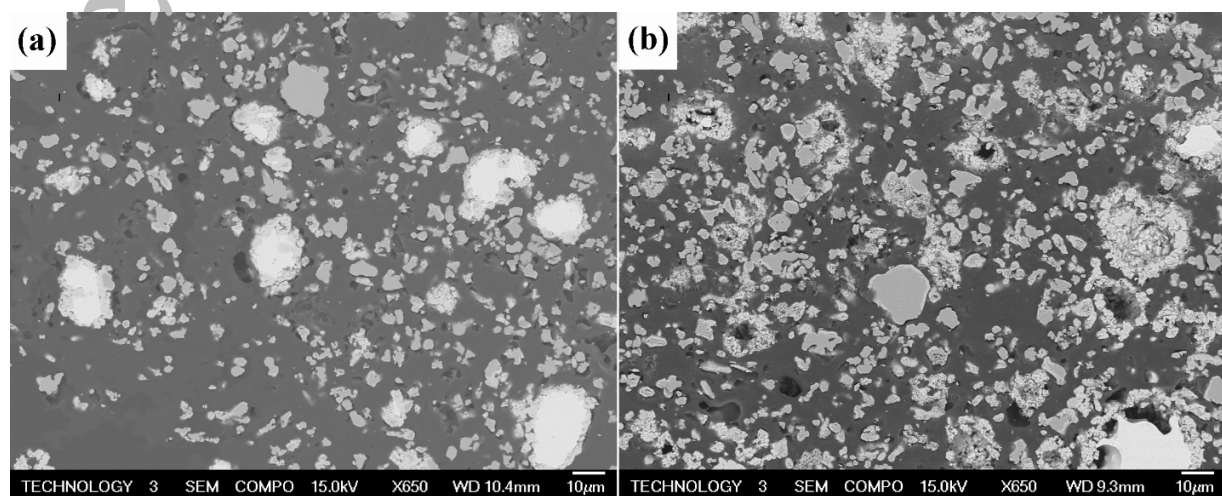


Figure 5. Representative SEM images of the composite sample (a) before annealing and (b) after annealing.

To provide further insight into the particle morphology and distribution changes during annealing, SEM analysis was conducted on polished cross sections of the composite before and after annealing, as shown in **Figure 5**. The hollow structures observed in Figure 5(b) are consistent with the tomography results, indicating that Sn originally contained in large Sn particles (higher absorption) is largely consumed during annealing, leaving shell-like structures behind. For sufficiently large Sn particles such as the one at the bottom right corner of Figure 5(b), the particle is not fully consumed, but provides evidence that the Sn is consumed from the outside to the inside.

Accepted Article

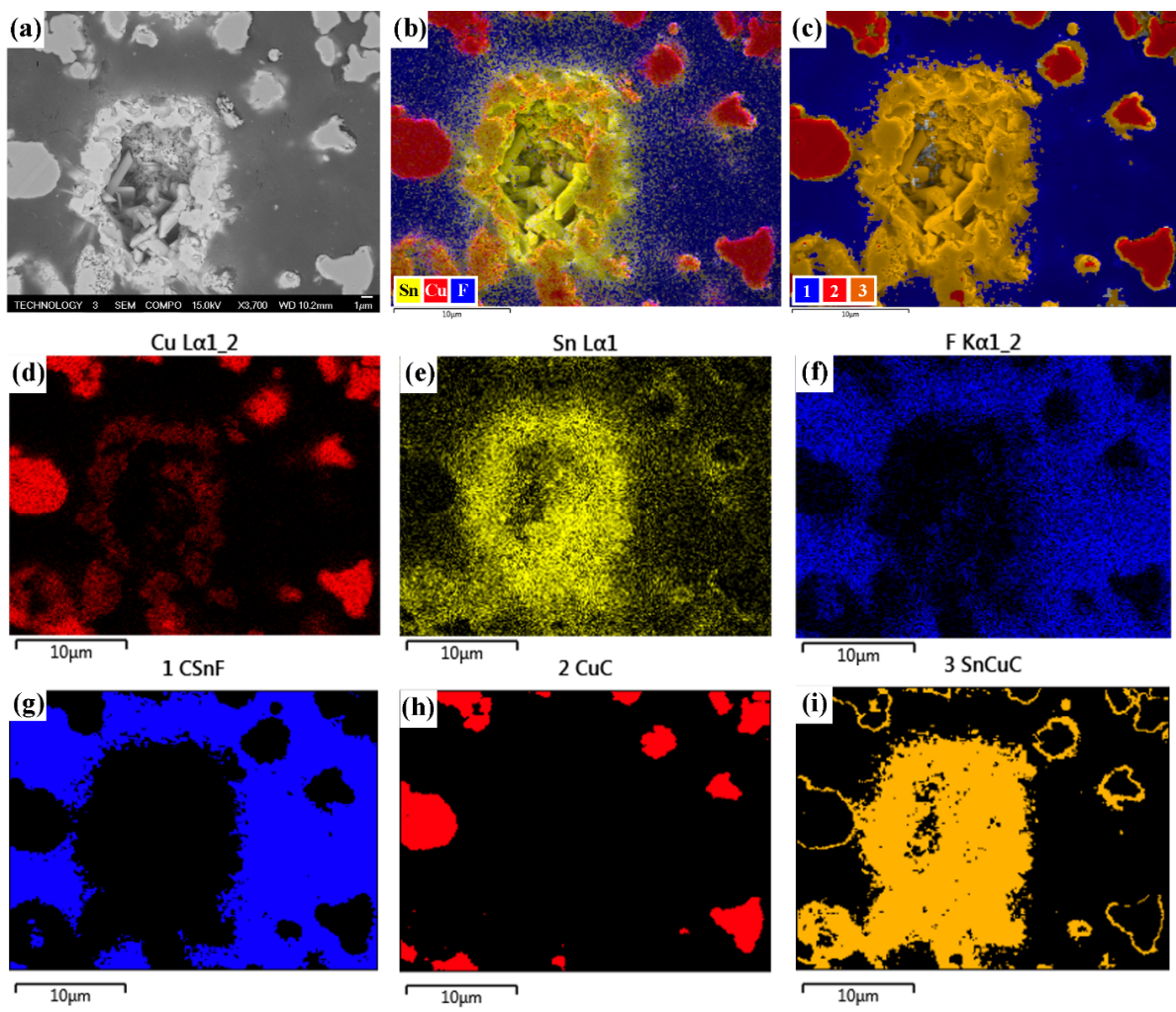


Figure 6. EDS maps of the post-annealed sample. (a) SEM image of the region of interest. Overlayed mapping of (b) elements and (c) phases of the region of interest. (d)-(i) Maps of individual elements (Cu, Sn, and F) and phases of interest identified by the software (CSnF(major composition: 60 at% C, 32 at% F, 4 at% O, 3 at% Sn), CuC (major composition: 53 at% Cu, 39 at% C), SnCuC (major composition : 41at% C, 19 at% Cu, 16 at% Sn)).

To investigate the elemental composition of the shell-like structures, EDS experiments were conducted on a representative feature and its surrounding area. As shown in **Figures 6(b)-(f)**, a shell structure containing primarily Sn is surrounded by scattered Cu particles. Figures 6(c)(g)(h)(i) display information relevant to the chemical phases present in the sample, which is

provided by the AZtecEnergy EDS software based on the relative EDS intensities for different elements. It is essential to understand that the “phase” concept here differs from the “phase” terminology referred in material science due to the fact that the AZtecEnergy software assigns different phases based on statistical differences between detected elemental intensities within each pixel. Therefore, the number of unique assigned phases can be impacted by image processing parameters such as boundary tolerance and grouping level. In this case, we used a medium level of boundary tolerance and group level to capture the distribution variation of material composition. For example, CSnF is not a real material phase, but the CSnF phase represented in Figure 6(g) shows the area where a combination of C, F, O and Sn was detected – this is the PVDF matrix, which has some Sn distributed throughout. As further example, CuC is not a real material phase, but the CuC phase represented in Figure 6(h) shows the regions where Cu and C were detected – these regions correspond to where metallic Cu is located. The C that was detected was likely present on the surface of the sample. Similarly, the CuSnC phase represented in Figure 6(i) corresponds to Cu-Sn intermetallic. The phase identifications suggest that the majority of the shell structure is composed of Cu-Sn intermetallic. Therefore, it seems that the large Sn particles present before annealing are consumed during annealing by the formation of Cu-Sn intermetallic shells, utilizing Cu from Cu particles originally surrounding the large Sn particles. Within the intermetallic shells that are formed, there seem to be random crystals as well as a porous fine structure, seen best in Figure 6(a).

Figure 6 also reveals that the Cu particles near the Cu-Sn shell structure have thin layers of Cu-Sn intermetallic around them, which form when Cu and Sn come into contact with one another at high temperature during compounding, molding, and annealing.

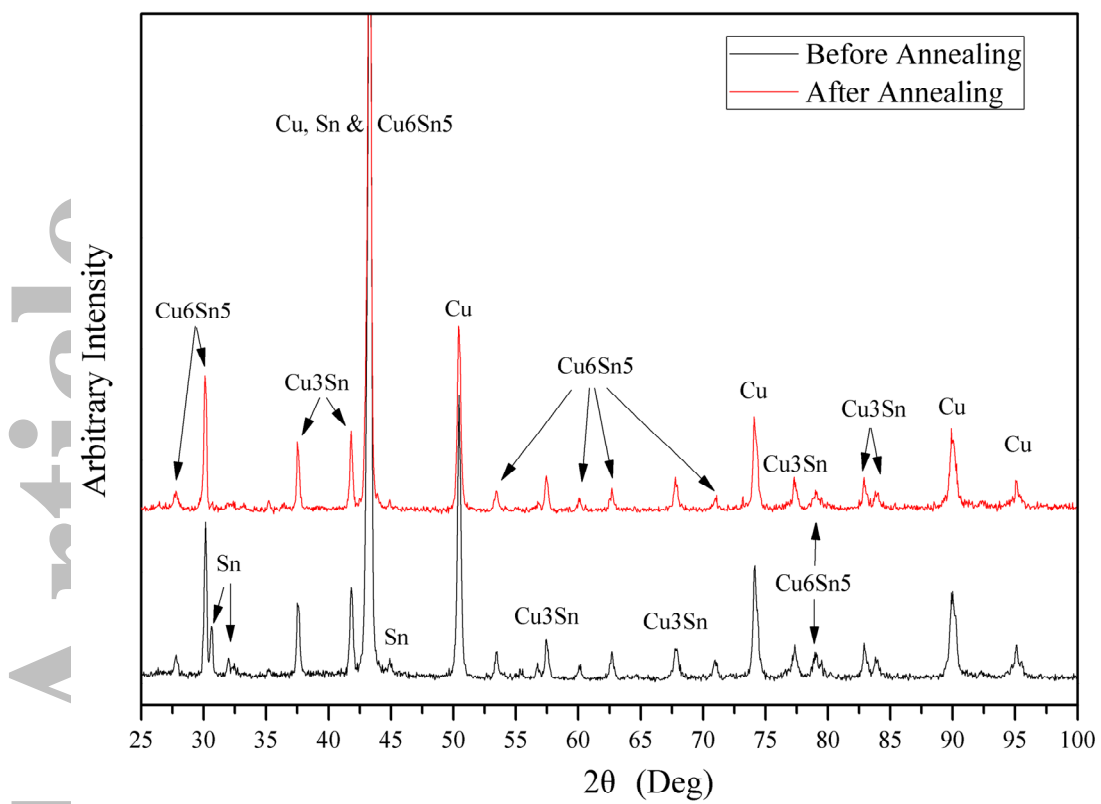


Figure 7. X-ray Diffraction (XRD) spectra of the composite sample before and after annealing

To further confirm the consumption of Sn and Cu for Cu-Sn intermetallic formation during annealing, XRD analysis was conducted on the composite sample before and after annealing.

The results are shown in **Figure 7**. Slight enhancements of the Cu₃Sn and Cu₆Sn₅ peak intensities were observed in the post-annealed sample (12% increase in Cu₆Sn₅ and 30% increase in Cu₃Sn according to peaking fitting using the Whole Powder Pattern Fitting (WPPF) method). At the same time, the Cu peak intensities are slightly decreased after annealing (7% decrease according to WPPF), indicating consumption of Cu. In addition, the reduction in peak intensity of the small peaks around $2\theta=31^\circ$, 32° and 45° provides further evidence for the consumption of Sn during annealing.

Conclusion

In-situ testing assemblies were designed to measure electrical resistance and perform X-ray tomography imaging of polymer composites filled with Cu and Sn during controlled thermal annealing. Changes in the 3D morphology and X-ray absorption of the composite were visualized and quantified throughout the annealing experiments. Generally, the dispersion of Sn is found to become more homogeneous during annealing, which is related to a corresponding reduction in resistance measured during similar thermal annealing conditions. In addition, SEM/EDS and XRD analysis provide detailed evidence for intermetallic Cu-Sn formation around Cu and Sn particles. This study provides detailed insight into the beneficial effect of annealing in Cu/Sn filler polymer composites in that high temperature and longer annealing time help the low-melting Sn particles to diffuse within the conductive network, presumably increasing the contact area between filler particles and thus enhancing electrical conductivity.

Acknowledgements

The authors would like to thank Michael Tang for running the MBIR tomographic reconstructions, Harold Barnard for help with in-situ test cell design, Dian Yu for helping with SEM/EDS, as well as Vishruth Mehta, Jaydip Das, Jerzy Gazda, Jim Toth and Nick Pugliano for helpful discussions. This work was supported by Tyco Electronics Corporation, a TE Connectivity Ltd. company. The X-ray Tomography facility at the Advance Light Source is supported by the Director, Office of Science, Office of Basic Energy Sciences, of the U.S. Department of Energy under Contract No. DE-AC02-05CH11231.

References

1. Bhattacharyya, S. K., Basu, S., De, S. K., Pal, A. K., Chowdhury, S. *J. Appl. Phys.*, **1978**, 49.
2. Garmabi, H., Naficy, S. *J. Appl. Polym. Sci.*, **2007**, 106, 3461–3467.
3. Deng, H., Skipa, T., Zhang, R., Lellinger, D., Bilotti, E., Alig, I., Peijs, T. *Polymer*, **2009**, 50, 3747–3754.
4. Garzón, C., Palza, H. *Compos. Sci. Technol.*, **2014**, 99, 117–123.
5. Chen, Y., Yang, Q., Huang, Y., Liao, X., Niu, Y. *Polymer*, **2015**, 79, 159–170.
6. Cipriano, B. H., Kota, A. K., Gershon, A. L., Laskowski, C. J., Kashiwagi, T., Bruck, H. A., Raghavan, S. R. *Polymer*, **2008**, 49, 4846–4851.
7. Yang, Q., Beers, M. H., Mehta, V., Gao, T., Parkinson, D. Y. *ACS Appl. Mater. Interfaces*, **2017**, 9, 958–964.
8. Wu, T., Pan, Y., Li, L. *J. Appl. Polym. Sci.*, **2011**, 121, 2969–2975.
9. Zhang, X., Pan, Y., Shen, L., Zheng, Q., Yi, X. *J. Appl. Polym. Sci.*, **2000**, 77, 1044–1050.
10. Zhang, X. W., Pan, Y., Zheng, Q., Yi, X. S. *J. Appl. Polym. Sci.*, **2000**, 78, 424–429.
11. Michaeli, W., Hopmann, C., Fragner, J., Pfefferkorn, T. *J. Polym. Eng.*, **2011**, 31, 479–487.
12. Mrozek, R. A., Cole, P. J., Mondy, L. A., Rao, R. R., Bieg, L. F., Lenhart, J. L. *Polymer*, **2010**, 51, 2954–2958.
13. Bormashenko, E., Sutovski, S., Pogreb, R., Sheshnev, A. In *Smart Structures and*

Materials 2002: Electroactive Polymer Actuators and Devices (EAPAD) **2002**; vol. 4695
465–472.

4. Bormashenko, E., Sutovski, S., Pogreb, R., Sheshnev, A., Bormashenko, Y., Levin, M., Westfrid, A. *J. Thermoplast. Compos. Mater.*, **2004**, 17, 245–257.
5. Pavlovic, M. M., Cosovic, V., Pavlovic, M. G., Talijan, N., Bojanic, V. *Int. J. Electrochem. Sci.*, **2011**, 6, 3812–3829.
6. Mamunya, Y. P., Davydenko, V. V., Pissis, P., Lebedev, E. V. *Eur. Polym. J.*, **2002**, 38, 1887–1897.
7. Mohan, K. A., Venkatakrishnan, S. V., Drummy, L. F., Simmons, J., Parkinson, D. Y., Bouman, C. A. In *2014 IEEE International Conference on Acoustics, Speech and Signal Processing* **2014**; 6959–6963.
8. Mohan, K. A., Venkatakrishnan, S. V., Gibbs, J. W., Gulsoy, E. B., Xiao, X., De Graef, M., Voorhees, P. W., Bouman, C. A. *Comput. Imaging, IEEE Trans.*, **2015**, 1, 96–111.
9. Doljack, F. In *IEEE Transactions on Components, Hybrids, and Manufacturing Technology* **1981**; vol. 4 372–378.
0. Antonova, K. V., Kolbunov, V. R., Tonkoshkur, A. S. *J. Polym. Res.*, **2014**, 21.